Physical and biological mechanisms for planetary waves observed in satellite-derived chlorophyll

Peter D. Killworth and Paolo Cipollini
James Rennell Division for Ocean Circulation and Climate, Southampton Oceanography Centre, Southampton, UK

B. Mete Uz
Earth System Science Interdisciplinary Center, University of Maryland, College Park, Maryland, USA

Jeffrey R. Blundell
James Rennell Division for Ocean Circulation and Climate, Southampton Oceanography Centre, Southampton, UK

Received 6 January 2003; revised 6 March 2004; accepted 31 March 2004; published 1 July 2004.

[1] We examine the evidence for global propagation of planetary wavelike features in sea-surface chlorophyll. Over much of the midlatitude ocean, westward propagating signals are seen that travel at the same speed as that predicted for long planetary waves. We then test three mechanisms for production of this signal. These are: horizontal (passive) north-south advection by the wave against a mean background gradient; vertical upwelling of nitrate, which is converted into chlorophyll; and vertical upwelling of chlorophyll itself. The tests involve comparisons of the amplitude and phase of the predicted signal with observations. The horizontal advective process predicts an amplitude for chlorophyll fluctuations that is in fair agreement with the data, though both overestimating and underestimating in places. The predictions for the phase difference between the chlorophyll and sea surface height signatures are in good agreement with the data. The upwelling biological mechanism could potentially give a large signal in the chlorophyll field, but the predicted amplitude patterns and the predicted phase difference (which is everywhere negative) are not in accord with the observations. Except in a few regions, the amplitude predicted by upwelling of chlorophyll is small compared with the horizontal advection mechanism. We conclude that over most of the ocean, the chlorophyll signal is well explained by horizontal advective processes, although we cannot rule out that there exist locations where additional biological mechanisms may be responsible for at least part of the signal. *INDEX TERMS:* 4572 Oceanography: Physical: Upper ocean processes; 4275 Oceanography: General: Remote sensing and electromagnetic processes (0689); 4279 Oceanography: General: Upwelling and convergences; 4855 Oceanography: Biological and Chemical: Plankton; *KEYWORDS:* planetary waves, ocean color, altimetry

Citation: Killworth, P. D., P. Cipollini, B. M. Uz, and J. R. Blundell (2004), Physical and biological mechanisms for planetary waves observed in satellite-derived chlorophyll, *J. Geophys. Res.*, *109*, C07002, doi:10.1029/2003JC001768.

1. Introduction

[2] The study of planetary waves (also known as Rossby waves) has made radical advances in the last few years, both on the observational and theoretical sides. These advances have been driven by the advent of large amounts of near-global satellite altimetric data and by the observed discrepancies between satellite-derived wave speeds and those from traditional theory [*Chelton and Schlax*, 1996], with waves seen propagating up to 3 times faster than the theory predicted. While there are several competing extended theories in existence, by far the simplest (and the one accounting for most, but not all, of the discrepancies) is that traditional wave theory neglects the existence of background mean flow in the ocean. This mean flow takes two forms. The natural choice is that the depth-averaged (barotropic) flow might Doppler-shift the westward flow. However, in most latitudes, the barotropic mean flow is believed to be far too small to have a noticeable effect on planetary wave propagation. (A notable exception is the eastward Antarctic Circumpolar Current, which is strong enough for waves to propagate eastward [*Hughes*, 1995].) Instead, the baroclinic mean flow (i.e., the mean flow less the depth-averaged mean) alters the local background potential vorticity gradient and, with it, the phase and group velocities of the planetary waves. *Killworth et al.* [1997] gave the first derivation of this, and computed expected wave speeds; *Dewar* [1998], *Liu* [1999], *de Szoeke and Chelton* [1999], and *Killworth and Blundell* [2003a, 2003b] have all extended or clarified the theory. Each wave solution takes the form of some vertical structure (a mode) that has a specific

0148-0227/04/2003JC001768

propagation speed. The fastest of these, the first mode, is the one that best fits most of the observed propagation.

[3] In parallel with the theoretical developments, satellite sensors have recently extended the range of quantities within which wave propagation can be seen (e.g., in sea-surface temperature; compare the global study by *Hill et al.* [2000], who found clear evidence of planetary wave propagation in all ocean basins). Somewhat surprisingly, planetary waves are also visible in maps of chlorophyll inferred from ocean color sensors [*Cipollini et al.*, 2001; *Uz et al.*, 2001]. The question we ask here is: What mechanism produces waves in ocean color? Two possibilities exist: purely physical processes and/or biological processes induced by physical processes.

[4] First, it is possible that the color signal is produced purely by physical processes, in this case, advection of chlorophyll. For long waves, the ocean can be thought of as having a rigid lid, so that advection at the surface is purely horizontal. In this case, a signal in chlorophyll can only appear if there are background horizontal gradients of chlorophyll. Consider, for instance, the situation depicted in Figure 1a, where a meridional (i.e., north-south) gradient of chlorophyll has been schematized as a front. In Figure 1b a field of westward propagating planetary waves has been superimposed on the background gradient; owing to geostrophic balance, there are meridional velocities of alternate sign on the wave sides, and these will eventually distort the front as displayed in Figure 1c, creating anomalies in the chlorophyll field that propagate westward alongside the waves.

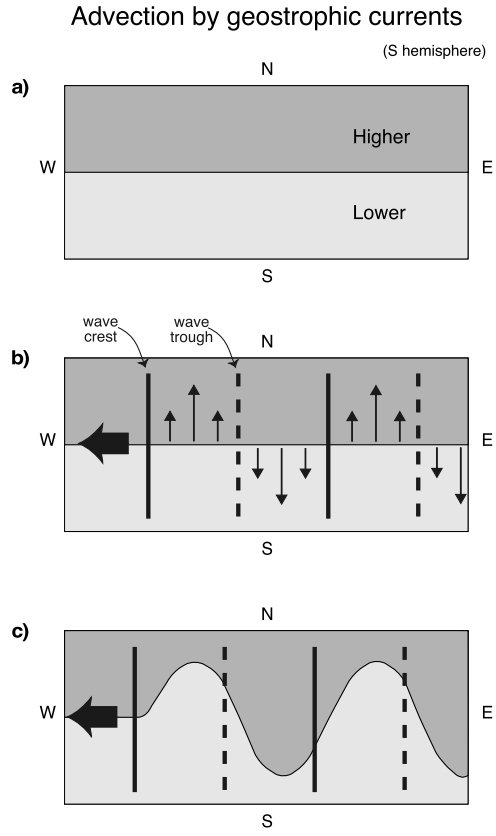

Figure 1. Scheme of the horizontal advection mechanism (advection of meridional gradients of a tracer by geostrophic velocities associated with planetary waves). (a) Background tracer field (gradient has been schematized as a front with higher concentrations to the North and lower to the South). (b) Tracer field with superimposed a planetary wave field and the associated geostrophic velocity field (indicated by the north-south arrows). The bold arrow shows the direction of propagation of the planetary waves. (c) A possible resulting perturbation in the tracer field (the phase relationship shown here is only qualitative; see section 3.2).

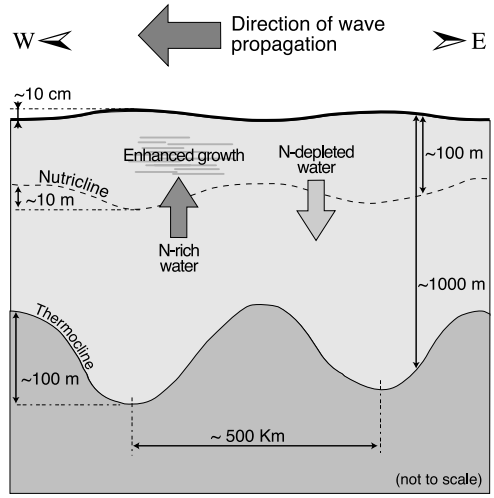

Figure 2. Scheme of the upwelling mechanism for a first mode-baroclinic planetary wave field, with the order of magnitude of the scales of the various features ("thermocline" indicates the midlatitude permanent thermocline).

[5] Another physical mechanism is the vertical advection of phytoplankton cells into or out of the surface mixed layer, which might simply make them more visible to an ocean color sensor and thus give a stronger chlorophyll signal, or drag them down and hide them from the sensor [see, e.g., *Charria et al.*, 2003].

[6] It is also possible that the signal is produced by biological processes (in turn induced by physical processes). Upwelling associated with a long planetary wave could bring additional nutrients into the turbulent mixed layer. These would be absorbed and converted to chlorophyll and so yield wavelike structures, propagating at the same speed as the planetary wave that generates them. A situation of this kind is sketched in Figure 2 for a first-mode baroclinic planetary wave. Even the aforementioned vertical advection of phytoplankton could trigger biological processes, such as enhanced or diminished growth due to the change in light availability over light-limited cell populations.

[7] As an alternative to dividing the possible mechanisms into purely physical and biological/physical, they can be classified as either horizontal or vertical. Vertical mechanisms like the upwelling described above would be of particular interest to biologists (indeed, most interactions of biology and physics have been traditionally couched assuming only vertical motion, which cannot be the case since vertical motion can only occur with concomitant horizontal motions). In fact, the waves could be one of the factors contributing to the balance between supply of nutrients to the upper layer and observed new production, a

balance that over large oligotrophic areas of the ocean has proven impossible to explain in terms of traditionally accepted mechanisms like winter convection, mixing at the thermocline, and wind-driven upwelling of nutrients [*Jenkins and Goldman*, 1985].

[8] Research carried out in the 1980s and 1990s has suggested that upwelling of nutrients by cyclonic mesoscale eddies (eddy pumping) could supply the missing nutrients [*Falkowski et al.*, 1991; *McGillicuddy et al.*, 1998]. Planetary waves might be playing a similar role, but with a key difference: While a cyclonic eddy retains water in its core and therefore upwells nutrients only when it forms or intensifies, planetary waves will pump nutrients upward on the leading side of the wave (in the thermocline or nutricline) all the way during their westward propagation across the oceanic basins, a mechanism dubbed the rototiller effect [*Siegel*, 2001]. Another possible mechanism could be the shoaling of the deep chlorophyll maximum and the subsequent mixing of cells in the mixed layer, as observed by *Kawamiya and Oschlies* [2001] at 12°S in the Indian Ocean.

[9] The present paper aims at investigating and, as far as possible, quantifying the mechanisms described above, by a combination of observations and modeling. Since the advent of satellite altimetry, sea surface height (SSH) has been used as the most direct method for global characterization of Rossby waves. Rossby waves induce small fluctuations in SSH (on the order of centimeters) that are much smaller than the modulation of thermocline depth (many tens of meters) but still measurable. We shall first use satellite measurements of SSH and ocean color to characterize the relationship between the physical waves and their biological manifestation by means of cross-correlation analysis. *Wilson and Adamec* [2002] have examined biophysical coupling using one-dimensional (1-D) correlations of SSH and ocean color time series at every location in the global ocean, and found the two quantities to be anticorrelated in most places; our 2-D cross-spectral analysis is complementary to their work in that it investigates the amplitude and phase relationship between westward propagating signals, excluding stationary signals as explained in section 2. We shall then model how this relationship should appear under each one of the mechanisms through which the physical wave could influence the biological field. A comparison of the modeled fields with the observations will allow us to assess which mechanism comes closest to reproducing the observations and to comment on the nature of the coupling between physical and biological effects of Rossby waves.

[10] The models we shall use are as simple as possible. Both the underlying physics and biology could be made much more complicated than our treatment here, but the complicated models bring with them a wide variety of parameters, often ill defined. We aim to look globally at the possible processes, with a minimum of parameters (and wherever possible, we will show that the variation of a parameter has little effect on our results, indicating that a more complicated model of the process represented by that parameter would produce similar results on the global scale). Until the simple models have been exhausted, there is little point in attempting complicated models.

[11] We shall use observations, rather than numerically modeled fields of SSH because, there being no firm agreement on the ways planetary waves are initiated and forced, wave properties such as amplitude and phase must be obtained directly from observation (SSH has by far the best data quality and coverage). Suppose, for example, the ocean color response were purely a result of the waves advecting chlorophyll (a possibility we examine quantitatively later). Models of planetary waves are capable of giving good predictions of wave speed, but, lacking the knowledge of forcing mechanisms, can give no direct predictions of phase or amplitude. Thus there is no direct way to predict the amplitude of any ocean color response produced by this mechanism without knowing the amplitude of the wave propagation. This in turn requires us to know the remotely sensed information about SSH.

[12] However, more is required than simply observed SSH amplitude. It is equally important to know how the phase of the color signal is related to that of the physical wave: Does it lead, or does it lag, the SSH signal? (That is, where on the physical wave is the highest chlorophyll concentration found: where SSH is maximum or minimum or on one of the flanks where geostrophic currents are strongest?) This information will be crucial in determining which mechanisms for the ocean color signal are more plausible.

[13] In this paper, then, we first analyze (in section 2) the observations of ocean color from the Sea-viewing Wide Field-of-view Spectrometer (SeaWiFS) [*McClain et al.*, 1998]. We compare these with altimetric sea surface height from the TOPEX/Poseidon (T/P) mission [*Fu et al.*, 1994]. The comparison is made by looking at the cross correlation and cross spectrum of filtered longitude-time plots of the two quantities, which allow an estimation of both the degree of similarity of the propagating features in the two data sets and their amplitude and phase relationship. Section 3 describes the modeling of two physical and biological mechanisms that may be responsible for the signature of planetary waves in ocean color, plus some variants on the mechanisms. In section 4 we discuss the results, by a comparison of observations and predictions of the various models.

2. Cross-Spectral Analysis of Chlorophyll and SSH

[14] This section describes some of the technical details of the data treatment, as well as the results of the analyses, on both the individual and combined data sets.

2.1. Ocean Color Data Preconditioning

[15] For the present study we have used SeaWiFS global area coverage (GAC) level 3 data from NASA Goddard Space Flight Center Distributed Active Archive Center (NASA-GSFC DAAC), processed by GSFC with version 4 chlorophyll algorithm [*O'Reilly et al.*, 1998]. The data are daily composites of chlorophyll (*chl*) concentration in mg/m^3 in Standard Mapped Image format, covering a period of almost 5 years from the start of the SeaWiFS mission (September 1997) to the end of the T/P data series available for comparison (early August 2002).

[16] Chlorophyll in the oceans tends to be lognormally distributed [*Campbell*, 1995], and it is often given in logarithmic form; therefore, as a first step in the analysis,

we took the decimal logarithm of the daily chlorophyll data. The $\log_{10}(chl)$ data were then rebinned in space from the original $0.0879^\circ \times 0.0879^\circ$ grid, far too detailed for observing large-scale features like Rossby waves, onto a 0.5°(longitude) $\times 1^\circ$ (latitude) grid, still sufficient to detect large-scale propagating signals. This additional binning reduces the noise and the effect of potential remnant cloud contamination on the data. The spatially binned daily data were then rebinned over the T/P orbital cycles (1 T/P cycle = 9.92 days), in order to have the two data sets on the same time grid for the cross-correlation analysis, and using the criteria of including in a cycle all the days covered (for at least 12 hours) by the cycle itself.

[17] We then extracted longitude-time sections (also known as Hovmöller diagrams) of the binned $\log_{10}(chl)$ and examined them for evidence of propagating waves. Features that propagate at a constant zonal speed describe a slanted straight line on a longitude/time plot. The slope of this line is inversely related to the propagation speed. Figure 3a shows, as an example, the unfiltered longitude time plot of $\log_{10}$-transformed chlorophyll concentrations along the entire parallel at 22°S. At a close look, anomalies can be seen to propagate westward across all the oceanic basins. These anomalies can be highlighted to some extent with a different choice of the color scale, but it is clear that filtering is necessary to properly isolate them from the variability due to other phenomena, such as local blooms and the seasonal cycle of phytoplankton. We first filled any residual gaps (mainly due to cloud coverage) in the global Hovmöller diagrams at each latitude with a Gaussian interpolation scheme in longitude and time, with full-width half maximum of 1.0° and 2 days and search radius of 1.5° and 20 days. The diagrams were then filtered with a westward only, band-pass 2-D filter with a 41×41 sample kernel passing 1.9° to 10.3° in space and 37 to 410 days in time. "Westward only" means that the band pass is situated only in the westward quadrants in wave number-frequency space (the transform of the longitude-time space). As a consequence, the filter effectively removes any eastward propagating signal as well as the seasonal cycle, any standing waves, and the high-frequency noise. The filtered longitude/time plot at 22°S is in Figure 3b, clearly displaying many westward propagating features with speeds between 4 and 6 cm/s in all three ocean basins. As the predicted error on the single 1-km SeaWiFS estimates of chlorophyll concentration is ±35% [*McClain et al.*, 1998], we can model the error as a Gaussian variable with standard deviation $\log_{10}(1.35)$, and produce a conservative estimate of the error on the gridded 10-day 0.5° $\log_{10}(chl)$ by assuming that at any step of the gridding process (1 km to 9 km, then 9 km to 0.5°, then 1 day to 10 day), only 20% of the data were valid (cloud free), which is certainly true over most parts of the ocean. This yields a standard deviation of the error on the final product $\epsilon \simeq 0.01$, proving that the features seen in Figure 3b are genuine propagating features in the ocean color field, well above the noise level.

[18] The $\log_{10}(chl)$ variance at the output of the westward only, band-pass 2-D filter is plotted in Figure 4a, expressed as percentage of the total $\log_{10}(chl)$ variance. In some regions of the Pacific subtropical gyres, it is higher than 20%, while at latitudes higher than 25°, it is almost everywhere less than 10% of the total variance, owing to the large amplitude of the annual cycle of phytoplankton at those latitudes. Figure 4b displays the same variance past the filter as in Figure 4a, but this time as a fraction of the residual variance; that is, the variance after the annual signal (estimated on a period of 4 years, 1998–2001) is removed from the data set at each location. From Figures 4a and 4b we conclude that westward propagating features in the 1.9° to 10.3° and 37 to 410 days range are a significant source of chlorophyll variability in the Pacific subtropical gyres, and are at least detectable in other regions once the annual phytoplankton cycle is removed.

2.2. SSH Data Preconditioning

[19] T/P ground tracks are spaced by 2.7° in longitude and repeated every orbital cycle of 9.92 days. We obtained along-track data in the form of the Geophysical Data Records from Archiving, Validation, and Interpretation of Satellite Oceanographic data (AVISO) and applied a standard set of corrections for orbit errors, atmospheric delays, tides, and sea state effects [see *Cipollini et al.*, 1997]. Then we computed the SSH anomalies (SSHAs) relative to the 1993–1995 mean height in each location along the tracks, and finally we used (cycle by cycle) a Gaussian interpolator in space, with a full-width half maximum of 150 km and a search radius of 200 km, to remap the data on a regular 1°longitude $\times$ 1°latitude $\times$ 1 cycle grid. The interpolation reduces the instrument and correction errors while leaving the larger-scale signal relatively unaffected. *Chelton and Schlax* [1996] suggest that signals with an amplitude of $\sim$1 cm may be observable. A total of 182 repeat orbit cycles were used (from cycle 183, coinciding with the start of the SeaWiFS data set in September 1997, to cycle 364 when T/P orbit was changed in early August 2002).

[20] Figure 3c shows the longitude/time plot of SSHA at 22°S. Westward propagating planetary waves with a speed of 5–6 cm/s (as expected from the extended theory at this latitude) are apparent in the plot even without filtering, especially in the Indian Ocean and in the western sector of the Pacific Ocean. However, for the correlation study, we chose to apply the same preconditioning to the two data sets; therefore the longitude/time plots of SSHA at each latitude were first reinterpolated to 0.5° in longitude (so that the grids of the two data sets become the same) and finally filtered with exactly the same westward only band-pass filter used for the chlorophyll data. The result of the filtering is in Figure 3d. Comparing this figure with Figure 3b, it can be seen that the features in the ocean color data set propagate with a similar speed to those seen in SSH data, and have similar length and timescale. In some locations, for instance in the Indian Ocean, the features in the two filtered data sets almost coincide. Comparison of SSH and

Figure 3. Examples of longitude-time plots of the chlorophyll and SSHA data sets, along the entire 22°S parallel. (a) Unfiltered $\log_{10}(chl)$. (b) Same as in Figure 3a, after filtering with the westward-only band-pass filter described in the text. (c) Unfiltered SSHA. (d) Same as in Figure 3c, after filtering with the westward-only band-pass filter.

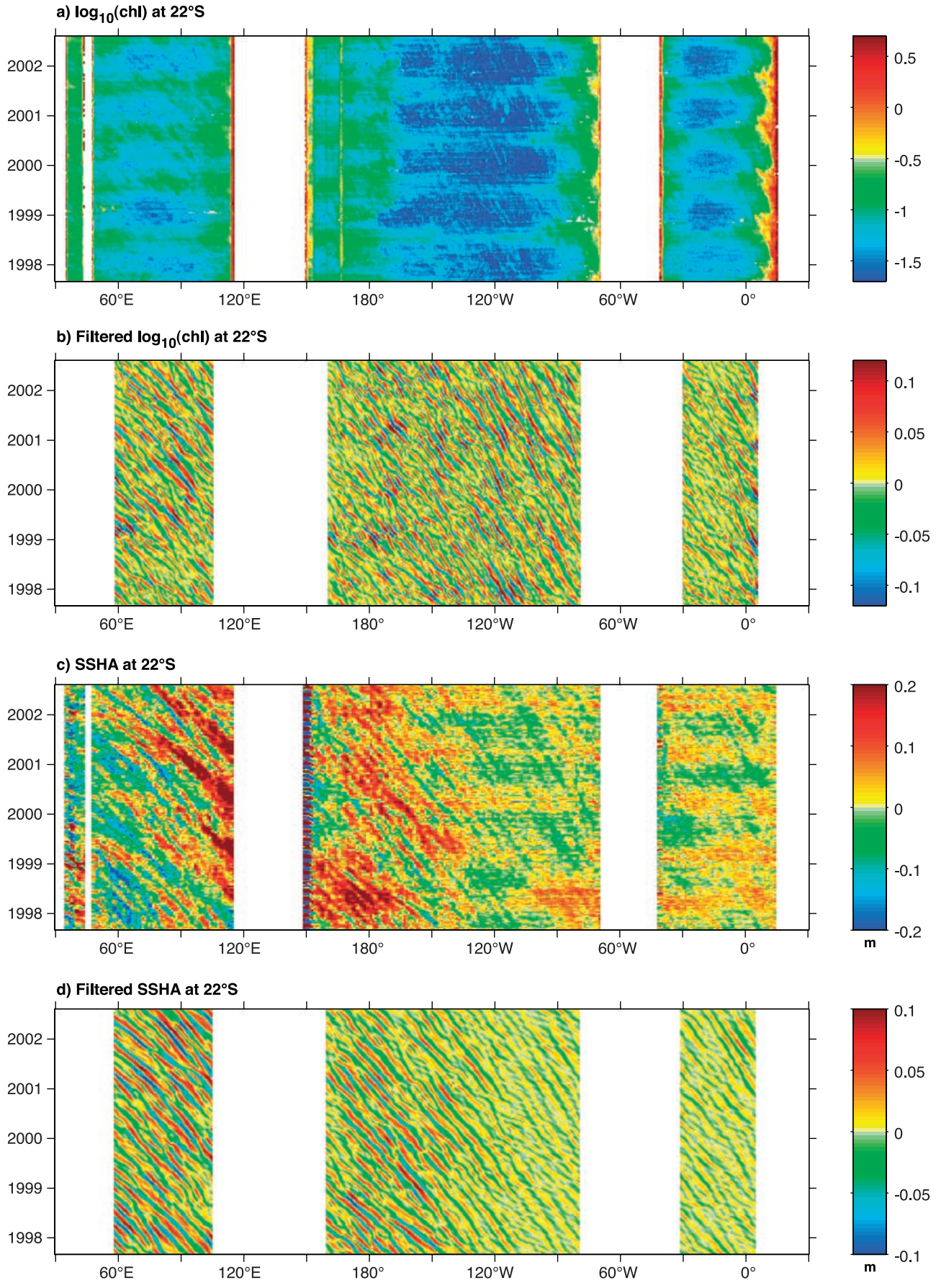
a) log10(chl) at 22°S
2002
2001
2000
1999
1998
60°E
120°E
180°
120°W
60°W
0°
0.5
0
-0.5
-1
-1.5
b) Filtered log10(chl) at 22°S
0.1
0.05
0
-0.05
-0.1
c) SSHA at 22°S
0.2
0.1
0
-0.1
-0.2
m
d) Filtered SSHA at 22°S

Figure 3

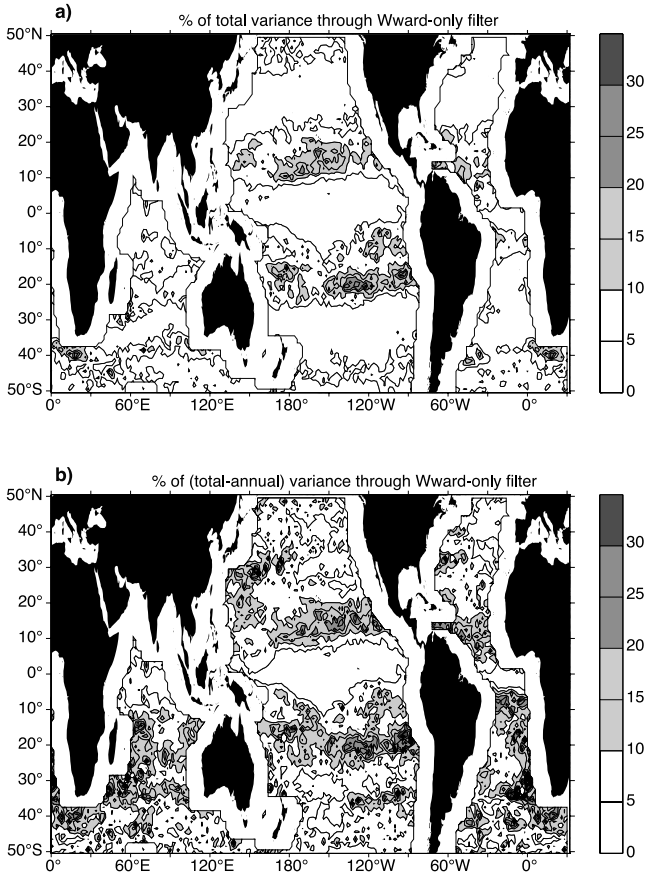

Figure 4. The $\log_{10}(chl)$ variance at the output of the westward-only, band-pass (1.9° to 10.3° in space and 37 to 410 days in time) filter (a) expressed as percentage of the total $\log_{10}(chl)$ variance, and (b) expressed as percentage of the total $\log_{10}(chl)$ variance minus the variance of the annual signal at each location.

ocean color at different latitudes (not shown here) confirms the findings by *Cipollini et al.* [2001] and *Uz et al.* [2001] that the signature of planetary waves is common in ocean color data, although filtering is very often required to separate it from other sources of variability.

2.3. Cross-Correlation and Cross-Spectrum Methodology

[21] In order to compute the cross correlation of the two data sets, we consider each location on a 2° longitude × 1° latitude grid over the ocean between 50°S and 50°N (which we will refer to as the analysis grid, chosen because this covers the latitude range in which most propagation is observed). For each analysis grid point, we select from the filtered longitude/time plots of both chl and SSHA a 20° longitude span centered on the grid point (corresponding to 41 points in the filtered data grid). Regions within 10° longitude from a zonal boundary are masked out in the analysis as land enters the longitude/time plots.

[22] For each pair of chl and SSHA longitude/time plots at an analysis grid point, we first compute the 2-D cross-correlation r_{ch}. As the filtered longitude/time plots have zero mean value (the zero-frequency, zero-wave number component has been filtered out), r_{ch} coincides with their covariance if r_{ch} is normalized, that is, divided by the square root of the product of the autocorrelations at zero lag (so that it is in $[-1, 1]$).

[23] The non-normalized 2-D cross correlations are then Fourier-transformed (with the 2-D FFT algorithm) to compute cross spectra, which in general are complex. The cross-spectrum amplitude (modulus) gives the joint power spectral density of the chl and SSHA longitude/time plots from which it is computed. Amplitude peaks in the cross spectrum will indicate those frequencies and wave numbers at which the two plots correlate best, and the corresponding phase will indicate the phase relationship of the two quantities at those frequencies and wave numbers, i.e., whether one is leading or lagging the other, and by how much. This kind of information from the chl-SSHA cross spectrum is very valuable in the process of assessing what are the mechanisms responsible for the propagating features seen in the chl data set, as we will discuss later.

[24] The above methodology is exemplified in Figure 5. Figures 5a and 5b show the filtered longitude-time plots of chl and SSHA, respectively, centered at 120°W, 22°S in the South Pacific Ocean, one of the regions with relatively higher cross correlation. Figure 5c shows the (normalized) cross correlation, having a positive peak of 0.53, and Figure 5d shows the cross spectrum, smoothed with a 3 × 3 spectral window, and its 90% confidence interval. The spectrum shows a significant peak at 0.152 degrees^{-1} and 2.64 yr^{-1}, corresponding to a wavelength of 6.58° and a period of 138 days. The phase in the peak (not shown) is 0.86 radians, corresponding to 19 days (the positive sign indicating that the signal in the $\log_{10}(chl)$ field leads the signal in the SSHA field).

2.4. Cross-Correlation and Cross-Spectrum Results

[25] The results for the cross-correlation and cross-spectral analysis are shown in the subplots of Figure 6. Figure 6a shows the maximum absolute value of the normalized cross correlation at each analysis grid point, giving a direct measurement of the degree of local similarity of the westward only features in the two data sets. The map of amplitude of the largest peak in the cross spectrum is in Figure 6b. The amplitude of the peak is an indication of how much of the correlation is due to periodic signals in the two data sets. Figure 6b shows similar features to those in Figure 6a in several regions of the world's oceans; however, there are also differences, as for instance in the North Pacific around Hawaii where the spectral peak is still relatively large, despite the cross correlation being small; this indicates that the little correlation that exists there is still largely due to a periodic signal. Period and wavelength corresponding to the largest cross-spectral peak in each location are in Figures 6c and 6d, respectively. In the 15°–35° zonal band, most of the signals that correlate best in the two data sets have periods of 120 days to semiannual, with wavelengths of a few hundred to about one thousand kilometers. Within 15° of the equator the analysis only finds short-period (less than 100 days) signals, certainly owing to (1) the wavelengths of propagating signals at these latitudes being larger than those allowed by the filter, and (2) the limited extent (20°) of the longitude window, which had to be chosen as a tradeoff between spectral resolution and localization of the analysis (needed for comparison with the

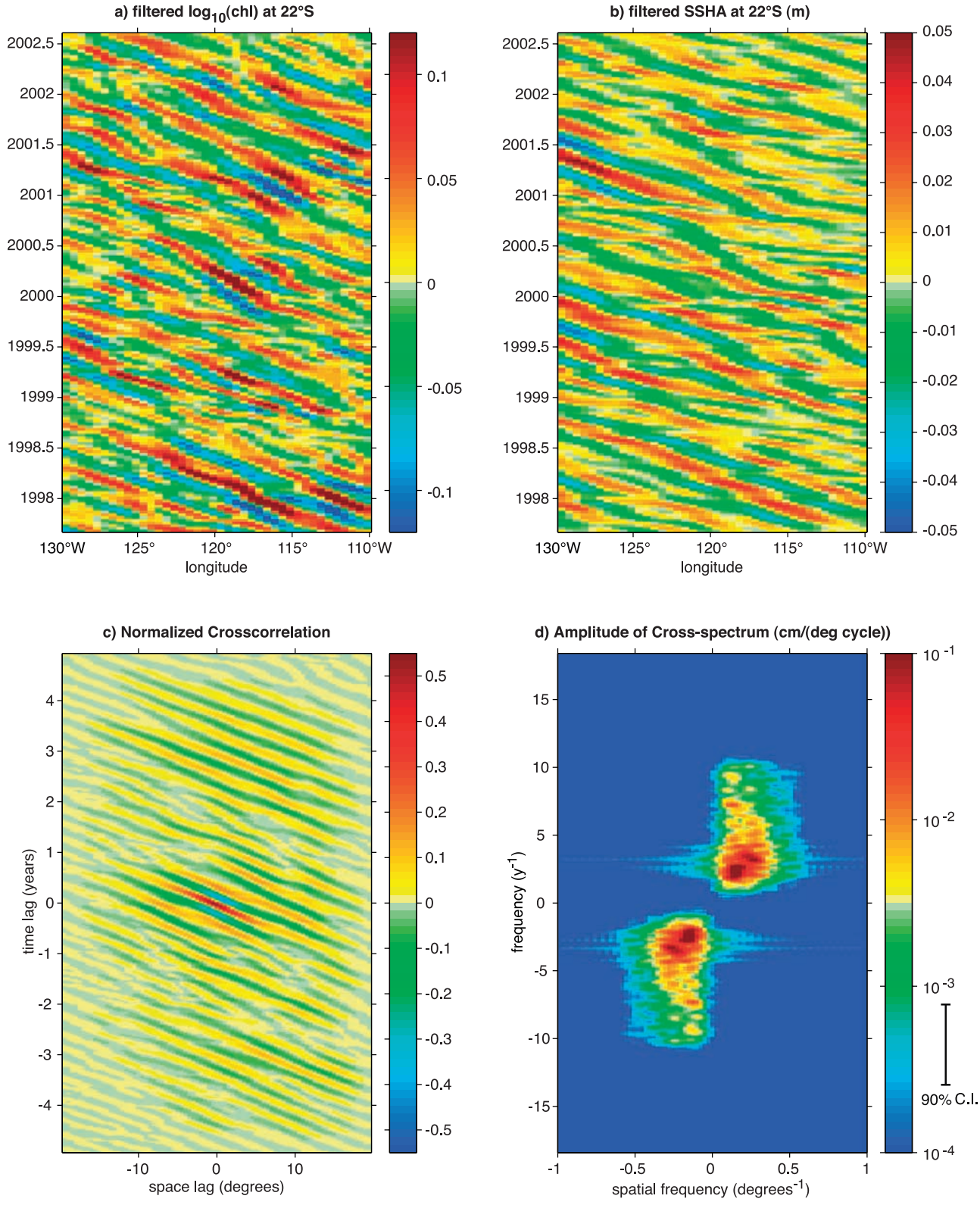

Figure 5. Example to illustrate the analysis methodology. (a) Filtered longitude/time plot of $\log_{10}(chl)$ centered at 120°W, 22°S in the South Pacific Ocean. (b) Filtered longitude/time plot of SSHA. (c) Normalized cross correlation of the plots in Figures 5a and 5b. (d) Cross-spectrum amplitude or joint power spectral density (modulus of the 2-D FFT of the cross correlation in Figure 5c), after filtering with a 3 × 3 window. The amplitude of the 90% confidence interval is also indicated to the right of the colorbar.

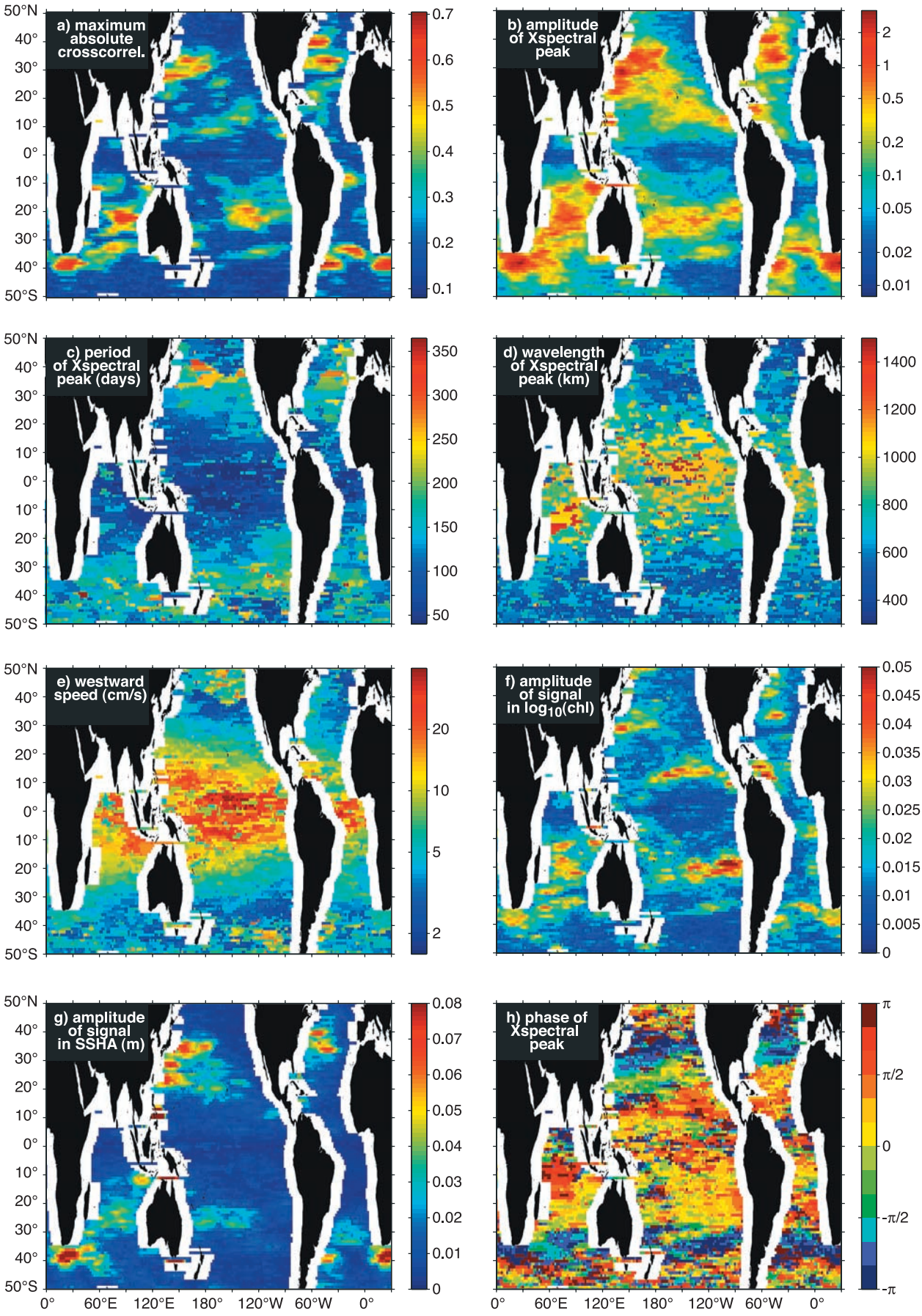
a) maximum absolute crosscorrel.
b) amplitude of Xspectral peak
c) period of Xspectral peak (days)
d) wavelength of Xspectral peak (km)
e) westward speed (cm/s)
f) amplitude of signal in log10(chl)
g) amplitude of signal in SSHA (m)
h) phase of Xspectral peak
50°N 40° 30° 20° 10° 0° 10° 20° 30° 40° 50°S
0° 60°E 120°E 180° 120°W 60°W 0°
0.7 0.6 0.5 0.4 0.3 0.2 0.1
2 1 0.5 0.2 0.1 0.05 0.02 0.01
350 300 250 200 150 100 50
1400 1200 1000 800 600 400
20 10 5 2
0.05 0.045 0.04 0.035 0.03 0.025 0.02 0.015 0.01 0.005 0
0.08 0.07 0.06 0.05 0.04 0.03 0.02 0.01 0
π π/2 0 -π/2 -π

Figure 6

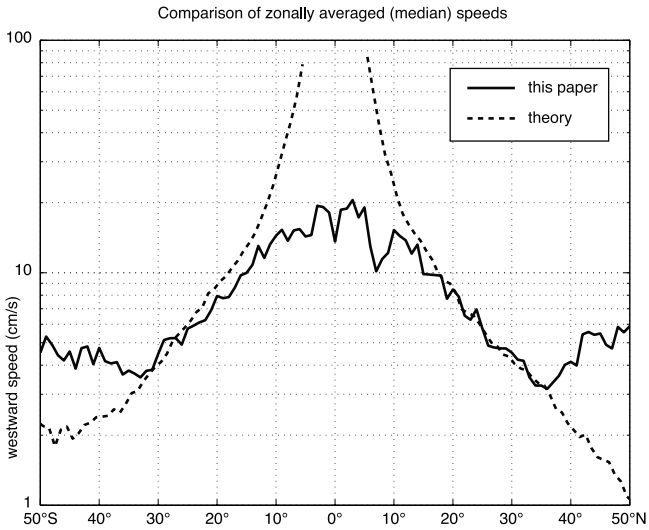

Figure 7. Comparison between the zonal median of the speed in Figure 6e (solid curve) and the zonal median of the speed predicted by the extended theory (from *Killworth et al.* [1997], recomputed with the climatological data by *Antonov et al.* [1998] and *Boyer et al.* [1998]).

model results, which are inherently local; see sections 3 and 4).

[26] Figure 6e shows the map of speed corresponding to the largest cross-spectral peak, and Figure 7 compares the zonal median of the speed with the prediction by the extended theory as used in section 3.2. The low (with respect to the theory) values of the observed speed within 15° of the equator could be due to the resolution problem outlined above. Figures 6e and 7 also show that poleward of 35° the correlation of chlorophyll and SSHA is mainly due to phenomena propagating significantly faster than planetary waves. In the 15°–35° zonal band the observed and predicted speeds are very close, and this is further evidence that most of the propagating signals seen in the ocean color data set in that latitude range are indeed due to planetary waves.

[27] Once the frequency and wavelength (and hence speed) of the peak in the cross spectrum are identified, we can estimate the power (and thus the amplitude) of the propagating signals in the two separate data sets by selecting the same frequency and wavelength in the auto-spectra (power spectral densities) of the single longitude/time plots, that is, the 2-D fast Fourier transform (FFT) of their autocorrelations. In practice, there may be spectral leakage of power into bins adjacent to the peak, so in the two auto-spectra we select a 3 × 3 cluster of spectral bins centered on the position of the peak in the cross spectrum, and we take the sums of the power values over the cluster and convert them back into amplitudes (the amplitude of the propagating signal in either $\log_{10}(chl)$ anomalies or SSHAs). Figure 6f shows the amplitude of the propagating disturbances (in the $\log_{10}(chl)$ data set) at the frequency and wavelength of the cross-spectral peak. It can be seen that in some regions (and notably, in significant part of the midlatitude Indian Ocean) the amplitude is ∼0.04, corresponding to chlorophyll concentration variations of about 10%. It should be noted that the numbers in Figure 6f are averages in both space and time (that is, over the 20° longitude span and ∼5-year time span used in the analysis); the amplitude of propagating anomalies in particular locations and times of the year can be larger, as visible in Figure 5a, which shows local variations of $\log_{10}(chl)$ of ±0.1 corresponding to chlorophyll concentration variations of ±25%.

[28] The amplitude of that part of the SSHA signal that correlates best with the chl signal is in Figure 6g. Note the 5-cm values across most of the Indian Ocean, and the higher values in the Agulhas region, in the Brazilian current region and in the western boundary currents of the Northern Hemisphere. Note also the tongue of increased values (up to 8 cm) at about 34°N in the North Atlantic, where previous research has found a "waveguide" of enhanced westward propagation [*Cipollini et al.*, 1997; *Cromwell*, 2001].

2.5. Use of Our Analyses as Tests of Models

[29] Comparison of amplitude is the usual test of agreement between modeling and observation. We note here that the phase relationship between the longitude/time plots of the two quantities ($\log_{10}(chl)$ and SSHA) also gives valuable clues as to what mechanisms are consistent with observations. Figure 6h displays a map of the phase of the cross-spectrum peak, that is, the phase between the chl and SSHA signals at those frequencies and wave numbers for which they correlate best. While in many areas poleward of 40° and close to the equator it is difficult to identify any clear features in the phase map (except perhaps for the phases around ±π in the North Atlantic), in the latitude range 10°–40° the map shows several regions of nearly constant or gradually varying phase plus some sharp transitions of approximately π. It is interesting to compare this map with the meridional gradient of the mean (over 1998–2001) of $\log_{10}(chl)$, computed from the same SeaWiFS data set and shown in Figure 8. These two maps show very similar patterns; in particular, several of the sharp π phase transitions in Figure 6h (like the one around 27°–28°N in the North Atlantic) coincide with sharp

Figure 6. Results from the cross-correlation and cross-spectral analysis. (a) Maximum absolute value of the normalized cross correlation of longitude/time plots of chl and SSHA. (b) Amplitude of the peak in the cross spectrum (cm · $degrees^{-1} cycles^{-1}$). (c) Period (days) corresponding to the peak in the cross spectrum. (d) Wavelength (kilometers) corresponding to the peak in the cross spectrum. (e) Propagation speed (cm/s, positive westward) corresponding to the peak in the cross spectrum. (f) Amplitude of the signal in the $\log_{10}(chl)$ field in a 3 × 3 bin cluster around the frequency and wave number of the cross-spectral peak. (g) Amplitude of the signal in the SSHA field in a 3 × 3 bin cluster around the frequency and wave number of the cross-spectral peak. (h) Phase of the peak in the cross spectrum, indicating the phase difference phase(chl)-phase(SSHA) between the propagating signals at the frequency and wave number of the cross-spectral peak.

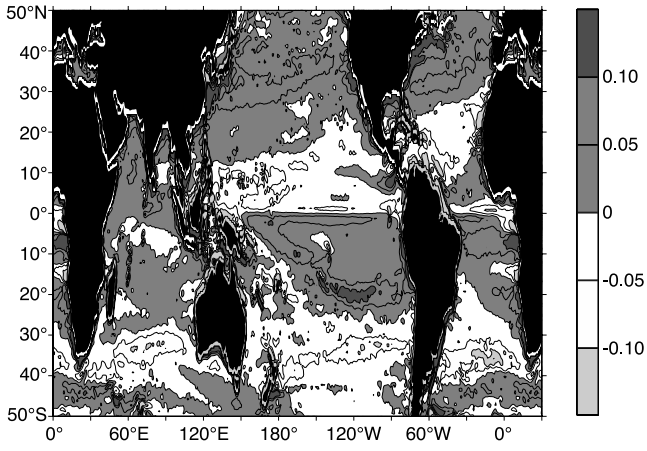

Figure 8. Meridional gradient (1/degree) of the mean (over 1998–2001) $\log_{10}(chl)$ from the SeaWiFS data set.

changes of sign in the gradient in Figure 8. A change of π in the phase relationship when the meridional gradient changes sign is exactly what one would expect from the advection mechanism outlined in Figure 1, as we shall show in section 3. This and other similarities between Figures 6h and 8 suggest that in several regions, horizontal advection must indeed be playing a role in the formation of a signal due to planetary waves in the chlorophyll data set, although it remains to be investigated whether it can explain the signal in its entirety.

[30] However there are other areas where the meridional gradients are weak, so that horizontal advection would not be a good candidate in these areas. Indeed, in some places (like between 20°N and 30°N in the Pacific Ocean) the phase relationship eludes immediate interpretation. From this preliminary look at the results it is obvious that we need to model the various possible mechanisms, and then compare both the relevant amplitude and phase relationships with those from the cross-correlation analysis, if we are to assess the relative contributions of each possible process at any location.

3. Modeling of the Physical and Biological Mechanisms

[31] We now turn to theoretical modeling of some possible processes generating the signal in ocean color. The phase and amplitude relationships modeled for these processes will be compared with the observed relationships in order to assess which process is dominant. The model involves small-amplitude perturbations to a steady (i.e., mean) state in which the ocean is in motion, and predicts the features of the first few vertical modes. We are mainly interested in the first vertical mode, as this propagates the fastest. The model we shall use has proven to give an accurate estimate of observed planetary wave speeds [*Killworth and Blundell*, 2003a], proving that the assumption of linearity within that model is quite reasonable. When this model is applied to biological tracers, the only potential nonlinearity lies in the biological interactions themselves; from the physical perspective the tracers are advected passively, and cannot affect the dynamics of the wave propagation.

[32] This section derives the predicted expressions for the effects on ocean color. Results and comparisons with observations are given in section 4.

3.1. Horizontal and Vertical Advective Effects

[33] We assume that the SSH η consists of a mean (background) part $\overline{\eta}$ and a wave perturbation η' (hereinafter, overbars denote means and primes denote perturbations). We write

$$\eta' = \eta_A e^{i\phi}, \phi = kx - \omega t, \tag{1}$$

where η_A is the wave amplitude and ϕ its phase. (Equation (1) is written in complex form; the signal is the real part only.) The wave is assumed to be propagating westward (in agreement with most observations), with wave number $k < 0$ and frequency $\omega > 0$; the axes are x east, y north, and z upward (with respective velocities u, v, w), and t denotes time. This definition has relevance to how we define phases, since at a given location the phase is decreasing, for an assumed positive frequency. Thus, to obtain the temporal phase shift between two signals, we need to compute minus the phase difference.

[34] Any north-south wave number (l) and phase variation ly are ignored. This is because (1) the data usually do not permit estimation of the north-south wave number l, and (2) realistic values of l make little difference to the answers. The latter is because [cf. *Killworth and Blundell*, 2001] the mean north-south flow tends to be weak compared with the mean east-west flow. Thus $\overline{v} = u' = 0$ in what follows.

[35] The wave is assumed long compared with the deformation radius (a characteristic length scale of order 30 km in most of the ocean), so that the predominant balance is geostrophic. Thus the northward perturbation surface velocity v_0' (the suffix 0 denoting surface values) is given by

$$v_0' = \frac{g}{f}\eta_x' = \frac{ikg}{f}\eta_A e^{i\phi}. \tag{2}$$

Here g is the acceleration due to gravity, and f is the Coriolis parameter. In the Northern Hemisphere, remembering that $k < 0$, the north-south velocity thus lags surface height (in x) and leads (in time) by $\pi/2$.

[36] Any tracer C satisfies the linearized version of the advection equation, which can be written

$$C_t' + \overline{u}C_x' + v'\overline{C}_y + w'\overline{C}_z = M, \tag{3}$$

where suffixes denote differentiation, M denotes an as yet unspecified mixing term, and we have substituted $C = \overline{C} + C'$. Here "mixing" is taken to include all processes that are nonconservative for the tracer. Readers uncomfortable with vertical variation within the mixed layer should note that upwelling into a slab mixed layer yields the same final equation.

[37] We wish to apply this equation at the surface of the ocean. The vertical advection presents a difficulty. In traditional planetary wave theory, the (very accurate) rigid lid approximation is made for convenience [*Gill*, 1982], so that w' vanishes identically at the surface. Nonetheless, vertical advection from beneath into a surface mixed layer, say, needs to be included somehow. We estimate w' at some

depth approximately that of the mixed layer from the vortex stretching equation

$$\beta v' = f w'_z, \tag{4}$$

where $\beta = df/dy$ is the northward gradient of the Coriolis parameter. (Equation (4) is obtained from cross differentiation of the geostrophic equations and use of mass conservation; the equation is valid for waves much longer than a deformation radius, here trivially true.) Integrating equation (4) from the surface to a depth h (assumed to be some mixed layer depth) gives

$$w'(z=-h) = -\frac{\beta h}{f} v'_0, \tag{5}$$

assuming that v' does not vary strongly through the mixed layer (which holds well for the first few vertical modes). We also write

$$h\overline{C}_z \equiv \overline{C}(z=0) - \overline{C}(z=-h). \tag{6}$$

(This would become less valid for larger h, but all available tracer data sets are only tabulated at discrete depths anyway.) We then approximate $w'\overline{C}_z$ by

$$w'\overline{C}_z = -\frac{\beta}{f} v'_0 \left(\overline{C}(z=0) - \overline{C}(z=-h)\right) \equiv -\frac{\beta}{f} v'_0 \Delta C, \tag{7}$$

using the shorthand $\Delta C \equiv \overline{C}\,(z=0) - \overline{C}(z=-h)$. This latter value can be considered as the value just below the mixed layer (since one would expect little variation across the mixed layer, although this expectation is not consistent with the available data sets). Indeed, as noted, an alternative formulation using divergences of fluxes and including upwelling into an explicit slab mixed layer gives identical results.

[38] This formulation has the disadvantage that it depends (weakly) on the choice of h. If the vertical gradient of $\overline{C}$ were uniform, the estimate for vertical advection would increase without limit as h increased. However, the ratio of vertical to horizontal advection,

$$\frac{\beta/f \Delta C}{\overline{C}_y},$$

is small for both chlorophyll and nitrate, for h up to about 50 m (according to the data sets referenced later in the paper), which is a reasonable upper bound for mixed layer depth in most of the ocean. For chlorophyll, the ratio is less than 0.2 except in the vicinity of sign changes in $\overline{C}_y$ and within about 10° of the equator. For nitrate, the same comment holds, but values are less than 0.1, except within about 5° of the equator. (However, the wave theory does not hold within about 5° of the equator anyway.) Thus, though our formulation for vertical advection is less than ideal, there should be little error given that the horizontal terms dominate. We give a quantitative example of the smallness of this ratio in section 4.

[39] Then, substituting equation (7) into equation (3), evaluated at the surface, gives

$$C'_{0t} + \overline{u} C'_{0x} + v'_0 \overline{C}_{0y} - \frac{\beta}{f} v'_0 \Delta C = -\frac{C'_0}{\tau}. \tag{8}$$

Here a further assumption has been made. The mixing has been simply parameterized as a return of the perturbation toward zero on some relaxation time τ. This timescale represents the aggregate of all processes that eliminate the nutrient anomaly. We are concerned with the total nutrient content, not just the dissolved concentration, and assimilation into biomass is not considered to be eliminating the nutrient anomaly. In fact, at the spatial/temporal scales of planetary waves, the assimilation of nutrients is effectively instantaneous. The loss of nutrients (and the consequent diminishing of the chlorophyll anomaly) happens through mixing or the sinking of particulate material such as large cells or fecal pellets out of the mixed layer. This assumption is certainly simple and in line with what we understand about the processes; we shall discuss values for τ later.

[40] The solution of equation (8) is

$$C'_0 = C_A e^{i\phi}, \tag{9}$$

where

$$-i\omega C_A + \overline{u}_0 ik C_A + \frac{ikg}{f}\eta_A \overline{C}_{0y} - \frac{\beta}{f}\frac{ikg}{f}\eta_A \Delta C = -\frac{C_A}{\tau}. \tag{10}$$

We shall assume that the phase speed c of the wave is known from theory or observations; it is negative, corresponding to westward propagation. The wave number k is given by

$$k = \frac{\omega}{c}. \tag{11}$$

Then, substituting for k,

$$\frac{C_A}{\eta_A} = \frac{g}{f}\frac{\left(\overline{C}_{0y} - \beta \Delta C/f\right)}{\left(c - \overline{u}_0 + ic/\omega\tau\right)}. \tag{12}$$

Expression (12) is sufficient to express the various possible combinations of mechanisms we shall be discussing; by omission of certain terms we can, for example, also restrict the dimensionality of the mechanisms, such as only considering vertical advection. Equation (12) is naturally written as an amplitude ratio, since, as noted above, we do not specify the formation mechanism for the waves and so η_A must be provided from observations.

[41] From the complex expression (12) it is straightforward to extract both the amplitude of C_A/η_A and the phase difference between C_A and η_A:

$$\text{Write } \frac{C_A}{\eta_A} = \left|\frac{C_A}{\eta_A}\right| e^{i\gamma} \tag{13}$$

[42] The spatial phase difference is given by

$$\Phi^x = (\text{phase}(C_A) - \text{phase}(\eta_A)) = \gamma, \tag{14}$$

[43] The temporal phase difference is

$$\Phi^t = -\gamma. \tag{15}$$

[44] Recall the discussion about spatial and temporal phase differences after equation (1). Note that phase differ-

ences other than zero or $\pm\pi$ are caused by the relaxation time τ.

[45] So far, we have not specified what tracer C represents. Depending on the mechanisms under consideration, the tracer may be chlorophyll (hereinafter also denoted by C; there will be no confusion), or nitrate (denoted by N).

[46] In what follows, we shall include or exclude various of the terms above. We shall also compute amplitude ratios and phase differences.

3.2. Physical Mechanism

[47] The basic physical mechanism, as noted, is to assume that horizontal advection of chlorophyll alone, against a north-south mean gradient, might account for the observations. To obtain this, we set ΔC to zero in equation (12), which removes the effects of vertical advection, giving

$$\frac{C_A}{\eta_A} = \frac{g}{f}\frac{\overline{C}_{0y}}{(c - \overline{u}_0 + ic/\omega\tau)}. \tag{16}$$

[48] There are two natural limits. The first is

$$\omega\tau \ll 1 (\text{fast decay}) \quad \frac{C_A}{\eta_A} = -\frac{ig}{fc}\overline{C}_{oy}\omega\tau. \tag{17}$$

Since $c < 0$, this gives the temporal phase of C_A' relative to η_A' as shown in Table 1. The amplitude of the ratio tends to zero for small τ.

[49] The second limit is

$$\omega\tau \gg 1 (\text{slow decay}) \quad \frac{C_A}{\eta_A} = \frac{g}{f}\frac{\overline{C}_{0y}}{c - \overline{u}_0}. \tag{18}$$

Since $c - \overline{u}_0 < 0$ [*Killworth and Blundell*, 2003a], the temporal phase of C_A' relative to η_A' is now as shown in Table 2. For large τ, the ratio becomes independent of the decay rate.

[50] Estimates of frequency and the size of the decay rate are required for evaluation of equation (16). We consider first the frequency.

[51] *Polito and Cornillon* [1997] provided SSHA-derived estimates of planetary wave frequency for the North Atlantic Ocean. Although there are small variations, the frequency is roughly annual between 17°N and 42°N, and so could be taken as constant. The estimates in this paper (Figure 6c), which show more variation in frequency with many observations around the semi-annual period, do not refer to the frequency of the dominant planetary wave signal in SSHA, but rather to the frequency of best correlation between the chl and SSHA signals. The joint chl/SSHA signal is exactly what we are modeling here, so we have chosen to use our estimates of frequency in the later computations.

[52] We use the phase speeds recomputed with the method of *Killworth et al.* [1997] but using the newer World Ocean Atlas 1998 data [*Antonov et al.*, 1998; *Boyer et al.*, 1998], as these have been shown to compare well with observations of planetary wave propagation.

[53] Finally, $\overline{u}_0$ is required. This is computed en route by *Killworth and Blundell* [2003a] from thermal wind balance, and temperatures and salinities from the World Ocean Atlas 1998 data [*Antonov et al.*, 1998; *Boyer et al.*, 1998]. The calculation ignores the barotropic flow, which is weak outside the Antarctic Circumpolar Current and does not have a strong effect on the wave speeds [*Killworth et al.*, 1997].

[54] Thus $\omega\tau$ can be estimated; in the subpolar regime it is about $5 \times 10^{-7}\tau$; in the subtropics, about $8 \times 10^{-8}\tau$. Three regimes thus appear: (1) fast decay everywhere: $\tau \ll$ 20 days; (2) intermediate decay (fast at low latitudes, slow at high latitudes): 20 days $\ll \tau \ll$ 150 days; and (3) slow decay everywhere: $\tau \gg$ 150 days. The fast and slow relaxation regimes can be conceptualized as follows. Consider a parcel of water that is within a gradient of tracer concentration and that has the same concentration as the waters around it. As the geostrophic velocity of an idealized Rossby wave moves this parcel meridionally, it will be carried against the gradient such that it is now surrounded by waters of a different concentration. If the relaxation is very slow, the parcel will practically retain its original tracer concentration and will present the largest anomaly relative to the ambient where it has reached the extremis of its meridional displacement. For a quasigeostrophic Rossby wave, this coincides with the largest SSH anomaly. If, on the other hand, relaxation is very fast, the parcel assumes the characteristics of the ambient as it goes, so that the only way to generate a strong anomaly is by moving the parcel very fast. Then the maximum anomaly will be observed along the flanks of the SSH anomaly where the pressure gradient (and therefore the geostrophic velocity) is strongest.

[55] Estimation of the relaxation time is difficult, since it can only be done by observing the evolution of an anomaly generated in the open ocean. Iron enrichment is one way of generating such an anomaly, and during the SOIREE experiment, sinking losses that translate to a relaxation timescale of 100 days have been observed [*Waite and Nodder*, 2001]. The longevity of the iron enrichment blooms may be partly because of major changes induced in the phytoplankton community structure, and 100 days may not be a representative value for the ocean in general. With ocean color remote sensing, we have observed τ values of 30 days for a bloom southeast of Madagascar and 10–20 days in the wake of a hurricane in the eastern Pacific (B. M. Uz and I. Ginis, manuscript in preparation, 2004). The cause of the Madagascar bloom is unknown, and τ observed here must reflect the slower of the decay rate of the causing agent and the intrinsic relaxation rate of chlorophyll anomalies. Thus 30 days is an upper bound on τ at this location. The observations over the cold wake of

Table 1. Temporal Phase of C_A' Relative to η_A' Given by Fast Decay Limit, Equation (17)

	$\overline{C}_{0y} < 0$	$\overline{C}_{0y} > 0$
Northern Hemisphere	$+\pi/2$	$-\pi/2$
Southern Hemisphere	$-\pi/2$	$+\pi/2$

Table 2. Temporal Phase of C_A' Relative to η_A' Given by Slow Decay Limit, Equation (18)

	$\overline{C}_{0y} < 0$	$\overline{C}_{0y} > 0$
Northern Hemisphere	0	$-\pi$
Southern Hemisphere	$-\pi$	0

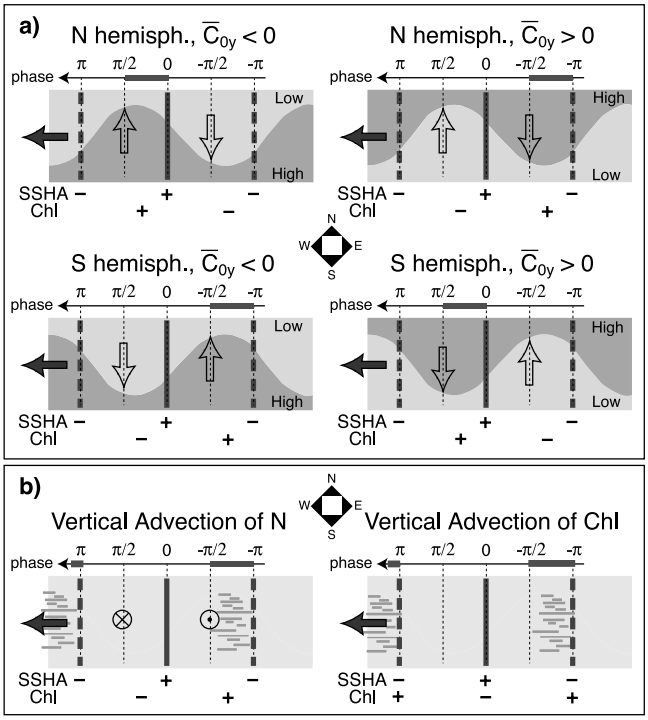

Figure 9. Scheme of phase relationship expected from (a) horizontal advection of chlorophyll and (b) vertical mechanisms. Planetary waves in SSHA are indicated by the thick north-south lines (solid line: crest; dashed line: trough). The bold arrows indicate the direction of propagation; open north-south arrows are the geostrophic velocities; gradients have been schematized as fronts. The thick segments on the phase axis indicate the expected temporal phase relationship.

a hurricane are perhaps the most direct way of estimating τ, but the data are very noisy because of cloudiness and the small amplitude of the chl anomaly. Thus it is not possible to determine τ very precisely. At the present time, 20 days is our best estimate for the relaxation time. Changing τ makes little difference to the results shown here (e.g., increasing τ increases the predicted amplitude ratio slightly and has a small effect on the phase), so that the crude approximation is not crucial to our findings.

[56] We take $\overline{C}_0$ as the mean of the SeaWiFS data over a period of 4 full years (1998–2001). This is obviously an approximation, as the satellite measurement will be an integral over some depth, but has the advantage of showing a much greater spatial detail than any available in situ surface chlorophyll climatology. The amplitude ratio and phase difference can then be computed from equation (16) using known data. (Note that results will be presented with a uniform value of the relaxation time of 20 days. Experiments with changing τ give results that agree with the predictions of equation (16).) Figure 9a gives a visual scheme of the phase relationship that can be expected from equation (16), for the different hemispheres and signs of $\overline{C}_{0y}$.

3.3. Biological Mechanism

[57] We now turn to a discussion of the biological mechanism. This, as normally stated, assumes that a linear wave induces upwelling of nitrates into the mixed layer, where they are converted into new chlorophyll (we assume that the conversion is immediate; this assumption is discussed in section 5). Nitrate satisfies equation (12), with C replaced by N, with both the explicitly horizontal flow and $\overline{N}_{0y}$ set to zero. Since w and v are intimately related by vortex stretching equations (4) and (5), this is not physically consistent unless the mean nitrate distribution is horizontally uniform.

[58] We must relate the amplitude of the chlorophyll signal to that of nitrate. An upper bound on this can be found by converting nitrate production (mmol N) to chlorophyll production (milligrams) by assuming a Redfield carbon/nitrate ratio of 6.625 (molar) and carbon/chlorophyll of 50 (g g^{-1}), giving a ratio of chlorophyll/nitrate bounded above by 1.59. This ratio has been frequently used elsewhere [e.g., *Kawamiya and Oschlies*, 2001]. This must overestimate the actual signal, but we are unaware of any method to estimate to what degree this occurs without the use of a model of considerably more complexity and with many adjustable parameters. Reducing the 1.59 value everywhere or just in some locations merely reduces the predicted ratio in such areas, and has no effect on the phase.

[59] Then we obtain

$$\frac{C_A}{\eta_A} = -1.59\frac{\beta g \Delta N}{cf^2}\frac{1}{(1+i/\omega\tau)}. \tag{19}$$

[60] (Note the factor f^2 in the denominator, indicating again the enhanced role of vertical motion near the equator.)

[61] Three difficulties of interpretation now become evident. First, nitrate can be both upwelled and downwelled. Under the traditional (biological) assumption that horizontal divergences may be neglected, downwelling induces no change to the nitrate supply in the mixed layer. The signal is therefore rectified, existing only when upwelling occurs (i.e., over half the wave cycle). *McGillicuddy and Robinson* [1997] discuss this effect. For our purposes, this is a simple example of a nonlinear response (rectification) to a linear process (upwelling). The calculation below ignores this, thus providing what is effectively an estimate of perhaps twice the observable signal. This is because the response is assumed to lie between $+M$ and $-M$ for some magnitude M, whereas the actual response would be between 0 and $+M$ only.

[62] Second, there are difficulties with nitrate data. While there are well-sampled local areas (HOT, BATS, etc.), these are of little help for our global study. However, in the *Conkright et al.* [1998] global data, fully half the ocean area is occupied by points in which annual mean surface nitrates exceed nitrates at 50 m. (The signal is remarkably noisy given the sparsity of the data sources and the degree of smoothing in the data reduction.) It is hard to see how the implicit reduction in nitrates could effectively be converted into chlorophyll. We therefore use the more recent data by *Louanchi and Najjar* [2001] in preference. These data have a more realistic depth distribution of nitrates, provided a mixed layer depth of 50 m is used, in that surface values are less than those at 50 m almost everywhere (in the following analysis the very few locations where this does not occur are masked off). Our operational choice of a mixed layer depth h of 50 m also appears as a realistic upper bound of the

depth of chlorophyll anomalies detectable in the SeaWiFS imagery; smaller values give similar diagrams, but with more masked out values for poor data. *Kara et al.* [2003] give a survey of mixed layer depths. We have run realizations for the biological mechanism(s) with h varying from 10 to 50 m, and the results depend very weakly on the value of mixed layer depth chosen.

[63] Third, nitrate levels in the upper ocean vary seasonally, yet we are compelled by data limitations to use the annual average since waves are visible at all times of the year. It is unclear what effect this would have on the results.

[64] Since c and ΔN are both negative (the latter by construction), the factor $\frac{\beta g \Delta N}{cf^2}$ in (19) is everywhere positive. Its amplitude and phase information can again be extracted

$$\left|\frac{C_A}{\eta_A}\right| = 1.59\,\frac{\beta g \Delta N}{cf^2}\sqrt{\left(\frac{\omega^2\tau^2}{1+\omega^2\tau^2}\right)}; \tag{20}$$

$$\Phi^t = -(\text{phase}(C_A) - \text{phase}(\eta_A)) = -\pi + \tan^{-1}(1/\omega\tau). \tag{21}$$

[65] Note that the temporal phase difference Φ^t takes the same value everywhere if τ and ω are assumed not to vary spatially. Even permitting both τ and ω to vary, the phase difference must lie between $-\pi$ and $-\pi/2$ and so cannot take both positive and negative values that are observed in Figure 6h: upwelling of nitrate induces chlorophyll variations that must lag the SSH signal (see Figure 9b for a schematic representation of the phase relationship). The two natural limits are as before,

$\omega\tau \ll 1$(fast decay)

$$\frac{C_A}{\eta_A} = i\omega\tau \cdot 1.59\,\frac{\beta g \Delta N}{cf^2}. \tag{22}$$

[66] The temporal phase of C'_A relative to η'_A is $-\pi/2$ in both hemispheres. The amplitude tends to zero for small τ.

$\omega\tau \gg 1$(slow decay)

$$\frac{C_A}{\eta_A} = -1.59\,\frac{\beta g \Delta N}{cf^2} \tag{23}$$

which is independent of τ for slow decay rates, and C'_A and η'_A are out of phase in both hemispheres.

[67] Now ΔN varies by a factor of 5–6 across the world ocean in the data set considered. Since an additional division by $\overline{C}$ is necessary to include the $\log_{10}$, the variation of $\overline{C}$ (by a factor of 10 across the ocean in the SeaWiFS data) also enters the amplitude ratio. Thus the amplitude ratio can vary strongly.

3.4. Variations of the Basic Models

3.4.1. Purely Vertical Advection of Chlorophyll

[68] *Charria et al.* [2003], using a radiative transfer model, have suggested that purely vertical advection of chlorophyll could account for the observed signal in the region of the South Atlantic Subtropical Convergence Zone where they carried out their analysis. It is straightforward to consider vertical advection of chlorophyll itself, although the calculation is forced to rely on annual averages of chlorophyll since these are all that are available subsurface in the data of *Conkright et al.* [1998]. The ratio is similar to equation (19), with chlorophyll substituted for nitrate, namely,

$$\frac{C_A}{\eta_A} = -\frac{\beta g \Delta C}{cf^2}\,\frac{1}{(1+i/\omega\tau)}. \tag{24}$$

When the relaxation time is very large (more accurately, when $\omega\tau \gg 1$), the chlorophyll signal is precisely π out of phase with the SSH, as discussed by *Charria et al.* [2003]. However, the phase changes as in the nitrate uplifting case when the relaxation occurs over a finite time, but is again always a phase lag (see Figure 9b).

[69] Unfortunately, the data quality is insufficient to yield reliable answers for equation (24). There are several locations in the *Conkright et al.* [1998] data (used consistently in this section for the vertical distribution of chlorophyll) where $\overline{C} = 0$ at the surface, which causes obvious difficulties when logarithms must be taken as before. Over the top 50 m, there are also many locations in which $\Delta C = 0$. However, we have argued earlier that the values predicted by this mechanism should be small compared with the horizontal advection mechanism; this will be demonstrated in section 4.

3.4.2. Fully Three-Dimensional Advection of Chlorophyll

[70] Advection is a three-dimensional process that has, slightly artificially, here been split into horizontal and vertical components (simply because the biological mechanism is traditionally posed as a purely vertical effect). The formulae above permit an evaluation of the predictions of a model that advects chlorophyll in all three dimensions; the amplitude ratio is given by equation (12). The evaluation suffers from the same data difficulties as before. The SeaWiFS measurements for $\overline{C}_{0y}$, and the *Conkright et al.* [1998] data for ΔC, will be used (accepting the shortcomings of the latter data set).

3.4.3. Fully Three-Dimensional Advection of Nitrate

[71] In exactly the same way, the full effects of advection can be considered for nitrate (i.e., adding horizontal advection to the existing biological model). The scaling arguments suggest that horizontal advection will completely swamp the vertical effects, and indeed values far in excess of observations are produced. Two comments may be made. First, it is unclear why surface nitrate has not already been converted to chlorophyll (so that why horizontal advection should trigger conversion is not obvious). Second, the uncertainty in the 1.59 factor (an upper bound) means that we can make no definitive statements as to the role of this process. No examples are given of this mechanism in the results section following.

4. Comparison of Observations and Model Results

4.1. Physical Mechanism

[72] We first compare observations and model results for the physical mechanism, i.e., the north-south advection of chlorophyll against a varying background mean chlorophyll distribution. The amplitude and phase predicted are given by equation (12). The amplitude ratio is shown in Figure 10a.

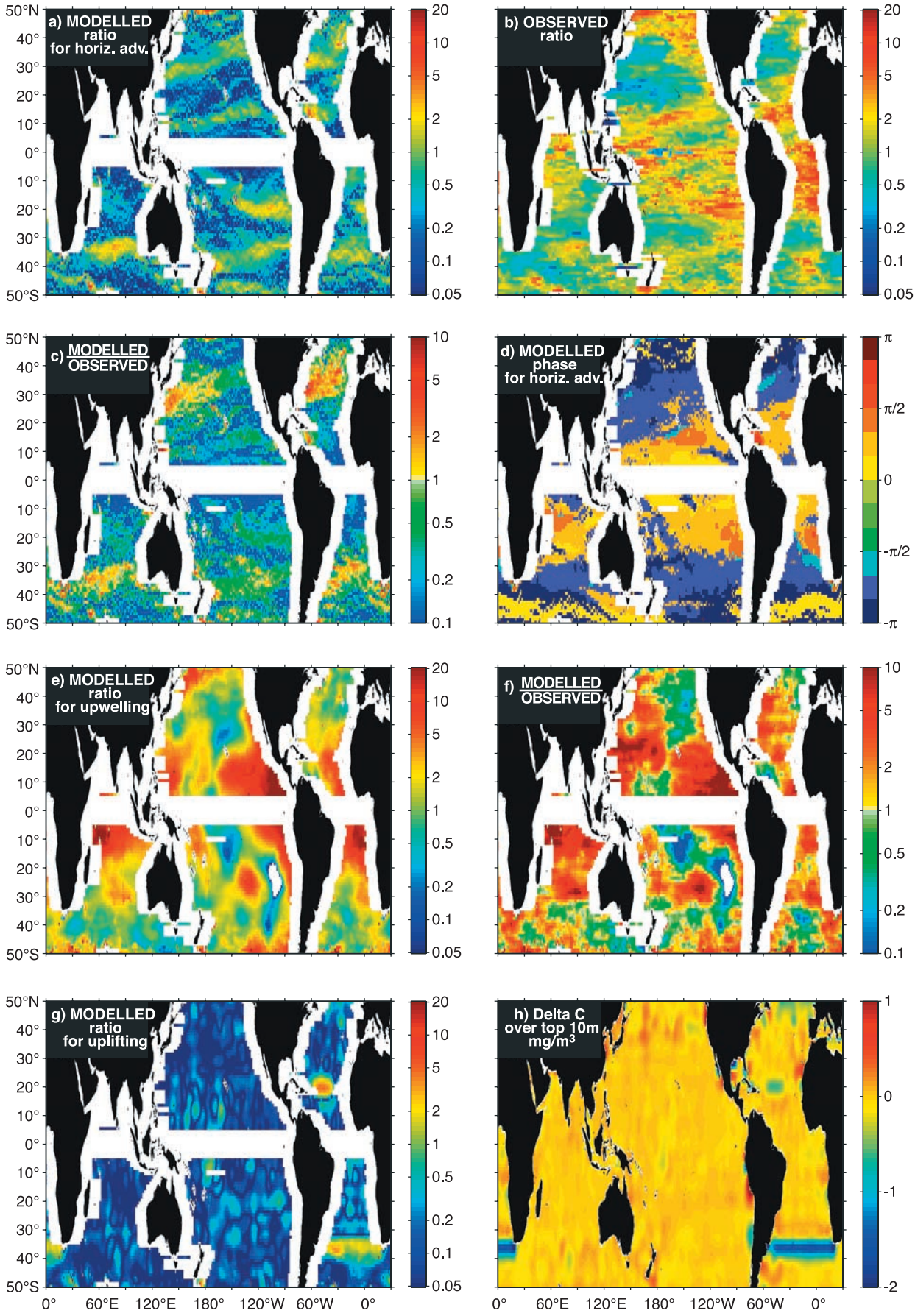
a) MODELLED ratio for horiz. adv.
b) OBSERVED ratio
c) MODELLED / OBSERVED
d) MODELLED phase for horiz. adv.
e) MODELLED ratio for upwelling
f) MODELLED / OBSERVED
g) MODELLED ratio for uplifting
h) Delta C over top 10m mg/m3
50°N 40° 30° 20° 10° 0° 10° 20° 30° 40° 50°S
0° 60°E 120°E 180° 120°W 60°W 0°
20 10 5 2 1 0.5 0.2 0.1 0.05
10 5 2 1 0.5 0.2 0.1
π π/2 0 -π/2 -π
1 0 -1 -2

Figure 10

The ratio is actually that of $(\log_{10}C)'/\eta_A$ to match the observations. (This can be computed either by using $\overline{\log C}$ for the background field, or by computing $C'/2.303\overline{C}$.)

[73] The predicted ratio is coherent over large scales, though it shows several "tongues" extending east-west across much of an ocean basin. The pattern shows several similarities to those found from the observations (Figure 10b). Direct comparison with the observations involves the comparison of one ratio with another (recall that our theory is couched as the ratio of chlorophyll to SSH). Thus the comparison, unfortunately, involves the ratio of two ratios.

[74] When we make this comparison (Figure 10c shows the predicted ratio divided by the observed ratio), the modeled amplitude ratio appears to be a little small over much of the world ocean, save a few "hot spots." The lowest values are found at midlatitudes (20°N–30°N, 25°S) in both data and theory. High values are found at high latitudes (the theory underestimating these somewhat), along eastern oceanic boundaries, in a tongue extending from Africa to the southern Caribbean, a tongue from South Australia to South Africa (overestimated by the theory), south of South Africa, around New Zealand, within the western boundary currents, and at several other locations, in both data and theory. The signal in the North Atlantic appears significantly overestimated by this theory.

[75] One noticeable area of difference is the considerable underestimation of the ratio by the theory within 10° of the equator. The theory assumes that the majority of the signal is comprised of the first (fastest) vertical mode. Interestingly, the second fastest mode, which does not exist with real frequency over about 50% of the ocean, does exist almost everywhere within 10° of the equator, and in these locations possesses a larger ratio of chlorophyll to sea surface height than does the first mode. While still smaller than observations, this is suggestive that higher modes may be playing a role near the equator.

[76] The temporal phase difference is shown in Figure 10d. Almost everywhere it falls in two intervals: $[0, \pi/2]$ at low latitudes (and in part of the Southern Ocean), and $[-\pi, -\pi/2]$ at high latitudes. This is consistent with the earlier discussion, and agrees extremely well with the phase difference from observations (Figure 6h). Both data and theory show sharp changes of about π (with some noise) as the meridional gradient of mean surface chlorophyll changes sign.

[77] Our model thus predicts a phase difference in striking agreement with the observed one and suggests that north-south advection against the background chlorophyll gradient, by the planetary waves, is responsible for most of the observed features in the chlorophyll wave data, although there are some discrepancies in the amplitude that require further explanation.

4.1.1. Purely Vertical Advection of Chlorophyll

[78] The predicted ratio is given by equation (24). *Charria et al.* [2003], using the same *Conkright et al.* [1998] data set as us, have shown that in the South Atlantic Subtropical Convergence Zone, a reasonably small upwelling velocity acting against a strong vertical gradient of chlorophyll over the top 10 m can produce a strong surface signal. This is in contradiction to our estimate in section 3.1, which shows vertical advection as weak compared with horizontal advection. Indeed, when equation (24) is computed globally using a mixed layer depth of 10 m for direct comparison with *Charria et al.* [2003] (Figure 10g), the amplitude ratio is almost everywhere small save in the region examined by *Charria et al.* [2003] and in a few other small regions. The reason for this can be found by examination of the vertical gradient of chlorophyll in the *Conkright et al.* [1998] data, accepting the shortcomings of those data. Figure 10h shows ΔC over the top 10 m, the measure employed by *Charria et al.* [2003]. It is clear that over most of the ocean this value is too small to exhibit a strong influence on the predicted signal. Hence simple vertical advection of chlorophyll is unlikely to be playing a significant role in the production of the color signal, except in a few localized areas.

4.1.2. Fully Three-Dimensional Advection of Chlorophyll

[79] The results (not shown) are almost identical to those for horizontal advection alone, as expected from the scaling arguments, demonstrating that vertical advection of chlorophyll is unlikely to play a large role in the observed wave signal compared with horizontal advection.

4.2. Biological Mechanism

[80] This mechanism, to recap, assumes that upwelling of nitrates into the base of the mixed layer, followed by conversion to new chlorophyll, can produce the observed signal. Equation (19) gives the predicted amplitude and phase.

[81] The amplitude ratio is shown in Figure 10e, and the value of the ratio divided by the observed ratio is shown in Figure 10f. The predicted ratio is almost everywhere either too small or too large (often it is far too large, which could be partly due to the upper bound effect discussed above). There are only a few areas of approximate agreement, most notably at high latitudes where planetary waves might not be the "best-correlated" signal in the spatial distribution of the amplitude ratio.

Figure 10. Results from the modeling and comparison with observations. (a) Ratio (amplitude of $\log_{10}(chl)$/amplitude of SSHA) predicted from horizontal advection of chlorophyll by the planetary waves. Chlorophyll is measured in mg/m^3; SSHA is measured in meters. A relaxation time of 20 days has been assumed. Values are masked within 5° of the equator where midlatitude planetary wave theory does not hold. (b) Ratio (amplitude of $\log_{10}(chl)$/amplitude of SSHA) from the cross-spectral analysis (ratio of Figures 6f and 6g). (c) Ratio of Figure 10a to Figure 10b. (d) Temporal phase Φ' of the predicted $\log_{10}(chl)$ relative to the SSHA, for a relaxation time of 20 days. (e) Upper bound for the amplitude of the predicted ratio (amplitude of $\log_{10}(chl)$/amplitude of SSHA) predicted from the biological mechanism (upwelling of nutrients by waves). The phase is not shown, as it is nearly constant and between $-\pi$ and $-\pi/2$. Masked values in the Southern Hemisphere indicate regions in which the nitrates at the surface exceed those at 50 m. (f) Ratio of Figure 10e to Figure 10b). (g) Amplitude of the predicted ratio for the chlorophyll uplifting mechanism, with a mixed layer depth of 10 m. (h) ΔC over the top 10 m from *Conkright et al.* [1998].

[82] The temporal phase difference is not shown, since its value is nearly uniform. We stress that while one can appeal to a spatially variable decay rate and/or frequency, it remains impossible to achieve a phase difference by this mechanism that achieves positive as well as negative phase lags (as seen in the observations) without appealing to a much more complicated mechanism. Therefore upwelling of nutrients due to planetary waves does not appear to provide an adequate explanation of the observed color signal.

5. Discussion

[83] This paper has examined physical and biological explanations for the observed westward propagation of features in ocean color data in as quantitative a manner as theory and data permit. Our first conclusion has been that the physical explanation, while far from giving perfect agreement with the data, provides a good explanation. In particular, the phase predictions of simple horizontal advection agree remarkably with the observations. (Given that the speeds in Figures 6e and 7 in the chlorophyll data are much larger at high latitudes than planetary waves, simple horizontal advection would be unlikely to give good agreement everywhere.)

[84] Conversely, a biological explanation based on upwelling of nitrates and a conversion to chlorophyll fails to give good estimates of the patterns observed in the amplitude of the signal, and predicts a phase for the signal which everywhere lags the sea surface height, which does not match the observations either. Of course, phytoplankton cannot assimilate new nutrients infinitely fast, as assumed by the biological model. However, the extra time lag for this process would be unlikely to be long enough to convert the existing (non-observed) global lag into a phase lead, since many months would realistically be involved.

[85] However, we cannot conclude that this mechanism does not happen: The upper bound for the predicted amplitude in Figure 10e is large over most of the oceans. The presence of planetary-wave induced upwelling would change the amplitude and phase relationship between the two variables and could still be responsible for some of the discrepancies between the observations and the predictions of the simple north-south advection mechanism.

[86] Our results can be compared with those of *Kawamiya and Oschlies* [2001], who studied the effect of planetary waves in a coupled physical, biological model at around 12°S in the Indian Ocean. They found surface chlorophyll anomalies only when the mixed layer is nearly as deep as the deep chlorophyll maximum (DCM); these anomalies are not produced near the surface, but result from the entrainment of chlorophyll from the DCM shoaled by the wave, suggesting that the generation of the surface chlorophyll anomalies may be sensitive to the dynamics of the mixed layer and DCM. In their example, the phase of the surface chlorophyll anomaly coincides with that of SSH, which is in contrast with our observational estimates for the area (we find that chlorophyll leads SSH by about $\pi/2$). It is hard to make a more formal comparison, as in situ data records are not sufficient to adequately constrain the vertical distribution of chlorophyll.

[87] It has also recently been suggested by *Dandonneau et al.* [2003] that the ocean color sensors may be reacting to particulate accumulation in convergence zones near the sea surface. While this process cannot be tested by the methodology adopted in this paper, it has been challenged by *Killworth* [2004], who showed that particles do not converge in a plane planetary wave.

[88] The main results of this study thus remain consistent: The simple north-south advection of the surface chlorophyll against its background gradient is sufficient to account for most of the observed propagation of waves in ocean color, but vertical mechanism could still be responsible for some effects, which call for further investigations. We suggest here two possible improvements. First, the modeling can be further refined both on the physics and the biology. Preliminary results by Farneti (personal communication, 2003) indicate that inclusion of vertical diffusion and energy balance surface boundary condition in the planetary wave analysis implies a phase shift in the perturbation horizontal velocity field which would modify the predicted relationship. Second, we can extend the analysis to other data sets. One particularly promising avenue of investigation is to add sea surface temperature (SST) data (compare the regional study by *Quartly et al.* [2003]), looking at the phase difference, or even the signed correlation between chlorophyll and SST. Since thermocline waters are cooler than the mixed layer, vertical mechanisms always result in low-SST, high-chlorophyll anomalies, while the result of horizontal advection varies depending on the relative direction of the gradients of SST and chlorophyll [*Uz and Yoder*, 2004]. This alternative method works over similar spatial and temporal ranges as the analysis reported here, but it is completely independent of SSH. Finally, a joint analysis of the signature of the single wave events in all the three data sets, SSHA, SST, and chlorophyll, will be required to identify precise times and places where vertical mechanisms may be significant.

[89] **Acknowledgments.** We are grateful to Peter Challenor, David Cromwell, Graham Quartly, Ian Totterdell, and David Woolf for their comments and suggestions. B. M. Uz was funded by NASA Office of Earth Science.

References

Antonov, J., S. Levitus, T. P. Boyer, M. Conkright, T. O'Brien, and C. Stephens (1998), *World Ocean Atlas 1998*, vols. 1–3, *Temperature of the Atlantic/Pacific/Indian Ocean, NOAA Atlas NESDIS 27*, 166 pp., Natl. Oceanic and Atmos. Admin., Silver Spring, Md.

Boyer, T. P., S. Levitus, J. Antonov, M. Conkright, T. O'Brien, and C. Stephens (1998), *World Ocean Atlas 1998*, vols. 4–6, *Salinity of the Atlantic/Pacific/Indian Ocean, NOAA Atlas NESDIS 30*, 166 pp., Natl. Oceanic and Atmos. Admin., Silver Spring, Md.

Campbell, J. W. (1995), The lognormal distribution as a model for bio-optical variability in the sea, *J. Geophys. Res.*, *100*, 13,237–13,254.

Charria, G., F. Mélin, I. Dadou, M.-H. Radenac, and V. Garçon (2003), Rossby wave and ocean color: The cells uplifting hypothesis in the South Atlantic Subtropical Convergence Zone, *Geophys. Res. Lett.*, *30*(3), 1125, doi:10.1029/2002GL016390.

Chelton, D. B., and M. G. Schlax (1996), Global observations of oceanic Rossby waves, *Science*, *272*, 234–238.

Cipollini, P., D. Cromwell, M. S. Jones, G. D. Quartly, and P. G. Challenor (1997), Concurrent altimeter and infrared observations of Rossby wave propagation near 34°N in the northeast Atlantic, *Geophys. Res. Lett.*, *24*, 889–892.

Cipollini, P., D. Cromwell, P. G. Challenor, and S. Raffaglio (2001), Rossby waves detected in global ocean colour data, *Geophys. Res. Lett.*, *28*, 323–326.

Conkright, M. E., T. O'Brien, S. Levitus, T. P. Boyer, J. Antonov, and C. Stephens (1998), *World Ocean Atlas 1998,* vols. 10–12, *Nutrients and Chlorophyll of the Atlantic/Pacific/Indian Ocean, NOAA Atlas NESDIS 36*, 245 pp., Natl. Oceanic and Atmos. Admin., Silver Spring, Md.

Cromwell, D. (2001), Sea surface height observations of the 34°N "waveguide" in the North Atlantic, *Geophys. Res. Lett.*, *28*, 3705–3708.

Dandonneau, Y., A. Vega, H. Loisel, Y. du Penhoat, and C. Menkes (2003), Oceanic Rossby waves acting as a "hay rake" for ecosystem floating byproducts, *Science*, *302*, 1548–1551.

de Szoeke, R. A., and D. B. Chelton (1999), The modification of long planetary waves by homogeneous potential vorticity layers, *J. Phys. Oceanogr.*, *29*, 500–511.

Dewar, W. K. (1998), On "too fast" baroclinic planetary waves in the general circulation, *J. Phys. Oceanogr.*, *28*, 1739–1758.

Falkowski, P. G., D. Ziemann, Z. Kolber, and P. K. Bienfang (1991), Role of eddy pumping in enhancing primary production in the ocean, *Nature*, *353*, 55–58.

Fu, L. L., E. J. Christensen, C. A. Yamarone, M. Lefebvre, Y. Menard, M. Dorrer, and P. Escudier (1994), TOPEX/Poseidon mission overview, *J. Geophys. Res.*, *99*, 24,369–24,381.

Gill, A. E. (1982), *Atmosphere-Ocean Dynamics*, 662 pp., Academic, San Diego, Calif.

Hill, K. L., I. S. Robinson, and P. Cipollini (2000), Propagation characteristics of extratropical planetary waves observed in the ATSR global sea surface temperature record, *J. Geophys. Res.*, *105*, 21,927–21,945.

Hughes, C. W. (1995), Rossby waves in the Southern Ocean: A comparison of TOPEX/Poseidon altimetry with model predictions, *J. Geophys. Res.*, *100*, 15,933–15,950.

Jenkins, W. J., and J. C. Goldman (1985), Seasonal oxygen cycling and primary production in the Sargasso Sea, *J. Mar. Res.*, *43*, 465–491.

Kara, A. B., P. A. Rochford, and H. E. Hurlburt (2003), Mixed layer depth variability over the global ocean, *J. Geophys. Res.*, *108*(C3), 3079, doi:10.1029/2000JC000736.

Kawamiya, M., and A. Oschlies (2001), Formation of a basin-scale surface chlorophyll pattern by Rossby waves, *Geophys. Res. Lett.*, *28*, 4139–4142.

Killworth, P. D. (2004), Comment on "Oceanic Rossby waves acting as a 'Hay Rake' for ecosystem floating by-products," *Science*, *304*, doi:10.1126/science.1094870.

Killworth, P. D., and J. R. Blundell (2001), Large-scale propagating disturbances: Approximation by vertical normal modes, *J. Phys. Oceanogr.*, *31*, 2852–2870.

Killworth, P. D., and J. R. Blundell (2003a), Long extra-tropical planetary wave propagation in the presence of slowly varying mean flow and bottom topography: I. The local problem, *J. Phys. Oceanogr.*, *33*, 784–801.

Killworth, P. D., and J. R. Blundell (2003b), Long extra-tropical planetary wave propagation in the presence of slowly varying mean flow and bottom topography: II. Ray propagation and comparison with observations, *J. Phys. Oceanogr.*, *33*, 802–821.

Killworth, P. D., D. B. Chelton, and R. A. de Szoeke (1997), The speed of observed and theoretical long extratropical planetary waves, *J. Phys. Oceanogr.*, *27*, 1946–1966.

Liu, Z. (1999), Forced planetary wave response in a thermocline gyre, *J. Phys. Oceanogr.*, *29*, 1036–1055.

Louanchi, F., and R. G. Najjar (2001), The mean annual cycle of nutrients and oxygen in the North Atlantic Ocean, *Deep Sea Res., Part II.*, *48*, 2155–2171.

McClain, C. R., M. L. Cleave, G. C. Fledman, W. W. Gregg, S. B. Hooker, and N. Kurig (1998), Science quality SeaWiFS data for global biosphere research, *Sea Technol.*, *39*, 10–16.

McGillicuddy, D. J., Jr., and A. R. Robinson (1997), Eddy-induced nutrient supply and new production in the Sargasso Sea, *Deep Sea Res., Part I*, *44*, 1427–1450.

McGillicuddy, D. J., Jr., A. R. Robinson, D. A. Siegel, H. W. Jannasch, R. Johnson, T. D. Dickey, J. McNeil, A. F. Michaels, and A. H. Knap (1998), Influence of mesoscale eddies on new production in the Sargasso Sea, *Nature*, *394*, 263–266.

O'Reilly, J. E., et al. (1998), Ocean color chlorophyll algorithms for SeaWiFS, *J. Geophys. Res.*, *103*, 24,937–24,953.

Polito, P. S., and P. Cornillon (1997), Long baroclinic Rossby waves detected by TOPEX/Poseidon, *J. Geophys. Res.*, *102*, 3215–3235.

Quartly, G. D., P. Cipollini, D. Cromwell, and P. G. Challenor (2003), Rossby waves: Synergy in action, *Philos. Trans. R. Soc. London, Ser. A*, *361*, doi:10.1098/rsta.2002.1108.

Siegel, D. A. (2001), The Rossby rototiller, *Nature*, *409*, 576–577.

Uz, B. M., and J. A. Yoder (2004), High frequency and mesoscale variability in SeaWiFS chlorophyll imagery and its relation to other remotely sensed oceanographic variables, *Deep Sea Res., Part II*, in press.

Uz, B. M., J. A. Yoder, and V. Osychny (2001), Pumping of nutrients to ocean surface waters by the action of propagating planetary waves, *Nature*, *409*, 597–600.

Waite, A. M., and S. D. Nodder (2001), The effect of in situ iron addition on the sinking rates and export flux of Southern Ocean diatoms, *Deep Sea Res., Part II*, *48*, 2635–2654.

Wilson, C., and D. Adamec (2002), A global view of bio-physical coupling from SeaWiFS and TOPEX satellite data, 1997–2001, *Geophys. Res. Lett.*, *29*(8), 1257, doi:10.1029/2001GL014063.

J. R. Blundell, P. Cipollini, and P. D. Killworth, James Rennell Division for Ocean Circulation and Climate, Southampton Oceanography Centre, European Way, Southampton, SO14 3ZH, UK. (jeff@soc.soton.ac.uk; cipo@soc.soton.ac.uk; pki@soc.soton.ac.uk)

B. M. Uz, Earth System Science Interdisciplinary Center, University of Maryland, 2007 CSS Building, College Park, MD 20742, USA. (uz@essic.umd.edu)